

Please cite the Published Version

Whitfield, D. , Baynes, E. R. C. , Hodge, R. A. , Rice, Stephen P.  and Yager, E. M. 
(2025) The Influence of Gravel-Bed Structure on Grain Mobility Thresholds: Comparison of Force-Balance Approaches. *Journal of Geophysical Research: Earth Surface*, 130 (5). e2025JF008333
ISSN 2169-9003

DOI: <https://doi.org/10.1029/2025jf008333>

Publisher: Wiley

Version: Published Version

Downloaded from: <https://e-space.mmu.ac.uk/639774/>

Usage rights:  [Creative Commons: Attribution 4.0](https://creativecommons.org/licenses/by/4.0/)

Additional Information: This is an open access article published in *Journal of Geophysical Research: Earth Surface*, by Wiley.

Data Access Statement: Data sets comprising gravel-bed microtopographies and field distributions for grain size, mass and resistance forces at each of the studied sites are available in the Zenodo repository (Whitfield et al., 2024).

Enquiries:

If you have questions about this document, contact openresearch@mmu.ac.uk. Please include the URL of the record in e-space. If you believe that your, or a third party's rights have been compromised through this document please see our Take Down policy (available from <https://www.mmu.ac.uk/library/using-the-library/policies-and-guidelines>)

The Influence of Gravel-Bed Structure on Grain Mobility Thresholds: Comparison of Force-Balance Approaches



Key Points:

- Two different novel force-balance models are used to estimate grain mobility thresholds using resistance force and microtopography data
- An automated point cloud segmentation approach is compared against a Monte Carlo approach which samples inputs from field distributions
- Site-average mobility thresholds are consistent with published values ($\tau_c^* = 0.05$ to 0.15). Both approaches produce similar τ_c^* estimates

Supporting Information:

Supporting Information may be found in the online version of this article.

Correspondence to:

D. Whitfield,
D.Whitfield@lboro.ac.uk

Citation:

Whitfield, D., Baynes, E. R. C., Hodge, R. A., Rice, S. P., & Yager, E. M. (2025). The influence of gravel-bed structure on grain mobility thresholds: Comparison of force-balance approaches. *Journal of Geophysical Research: Earth Surface*, 130, e2025JF008333. <https://doi.org/10.1029/2025JF008333>

Received 6 FEB 2025
Accepted 15 APR 2025

D. Whitfield¹ , E. R. C. Baynes¹ , R. A. Hodge² , S. P. Rice³ , and E. M. Yager⁴ 

¹Geography and Environment, Loughborough University, Loughborough, UK, ²Department of Geography, Durham University, Durham, UK, ³Department of Natural Sciences, Manchester Metropolitan University, Manchester, UK, ⁴Department of Civil and Environmental Engineering, Center for Ecohydraulics Research, University of Idaho, Boise, ID, USA

Abstract Grain force-balance models utilize grain protrusion and in-situ resistance force data to evaluate the likely distributions of gravel-bed sediment entrainment thresholds, specifically dimensionless critical shear stress (τ_c^*). These methods can give insight into the spatial variability of particle mobilities both within a channel, and between different gravel-beds, but are yet to be evaluated across multiple sites with varying texture and fabric. We evaluate two published force-balance approaches: (a) a Monte Carlo style sampling approach using grain size and topography distributions from field measurements; and (b) an automated point cloud segmentation and analysis approach with an updated set of force-balance equations, Pro+. We compare the workflows, assumptions and inputs for each approach, apply them to an extensive UK-wide data set comprising 45 upland riverbeds, and evaluate the estimated τ_c^* distributions. We find that mobility thresholds estimated from both methods are variable, with median τ_c^* ranging from 0.05 to 0.15, and are consistent with published values of approximately 0.02–0.1. Uncertainties in grain sampling strategy or point cloud segmentation quality lead to markedly different grain size distributions between approaches, but their resulting influences on τ_c^* distributions are small relative to the range of estimated τ_c^* . Sensitivity analyses on τ_c^* distributions for grain-size fractions also show that bed mobilities are sensitive to the roughness height of the velocity profile. We highlight uncertainties associated with these approaches, suggest areas for further targeted comparisons between methods, and provide guidance for the application of grain force-balance models for estimating entrainment thresholds and bed stability in gravel-bed rivers.

Plain Language Summary The forces required to mobilize riverbed material in gravel-dominated rivers is important in understanding whether a river is likely to erode into its bed. This force is typically assumed, based on how steep the river is, or how large the material is. We test two process-based approaches, which evaluate the forces acting on a single grain to estimate the forces required to transport it, using data acquired from field measurements and 3D digitized riverbeds. The first approach randomly selects inputs from data observed in the field to evaluate different combinations of gravel sizes, arrangements and stabilities that are most likely to be observed in the field. The second approach automatically identifies individual grains and extracts real data for each identified gravel to estimate the forces required to begin grain movement. We perform each method on 45 upland rivers across the UK, compare their predicted erosion thresholds, and discuss potential limitations and sensitivities for each approach. Our estimated bed erosion thresholds are consistent with those used in other studies but enable a smaller-scale evaluation of their variabilities (e.g., variabilities within rivers, rather than assuming a value for an entire channel), which can be useful in river management.

1. Introduction

Understanding the mobility thresholds of river bed material, and their spatial variability gives insight into the erodibility of a channel bed, and therefore assists in predicting bed stabilities, upstream sediment supply rates (Mao, 2012; Recking, 2012; Venditti et al., 2010), and ultimately aids in predicting channel adjustment (Chapman et al., 2021; Dunne & Jerolmack, 2020; Métivier et al., 2017; Parker et al., 2007; Pfeiffer et al., 2017; Phillips et al., 2021). In gravel-bed rivers, grain mobility thresholds are quantified using the dimensionless critical shear stress or Shield's criterion (τ_c^*); the force per unit area required to initiate bedload transport is normalized by the submerged grain weight. In sediment transport modeling applications, and in geomorphic theory, such as equilibrium channel geometry theory, τ_c^* is generally assumed to be controlled by channel slope (Lamb et al., 2008; Recking, 2009) and/or particle grain size (Buffington & Montgomery, 1997; Bunte et al., 2013; Wilcock, 1993).

© 2025. The Author(s).

This is an open access article under the terms of the [Creative Commons Attribution License](https://creativecommons.org/licenses/by/4.0/), which permits use, distribution and reproduction in any medium, provided the original work is properly cited.

However, such predictions still have considerable uncertainties, which at least in part is because they neglect the influence of grain-scale sediment structure and bed resistance forces on sediment mobility thresholds.

The resulting uncertainties in values of τ_c^* are problematic because sediment flux is sensitive to subtle variations in τ_c^* (e.g., Recking, 2010; Wilcock, 1993), with consequent issues for modeling bedload transport rates, and in predicting channel morphological change and associated hazards. Spatial and temporal variabilities of τ_c^* in gravel-bed rivers are difficult to quantify in the field without long term sediment flux monitoring, for example, using sediment impact plates or tracer particles (Downs & Soar, 2021; Masteller et al., 2019; Smith et al., 2023; Turowski et al., 2011) in conjunction with local hydraulic measurements or estimates. Furthermore, studies which investigate the linkages between sediment arrangement, τ_c^* and sediment flux are largely limited to experimental channel beds (Hodge et al., 2020; Ockelford et al., 2019; Voepel et al., 2019). However, controlled laboratory channels typically cannot holistically address real-world sensitivities which contribute to τ_c^* variability, such as sediment supply intermittency, flood sequencing, and biological influences. Consequently, it is difficult to accurately predict the erodibility of channel beds over various scales, and to incorporate realistic bed mobility threshold and sediment flux estimates into channel evolution models.

Grain force-balance models (Kirchner et al., 1990; Hodge et al., 2013; Yager et al., 2018; see Section 2) enable the resistance of a grain to transport to be evaluated by resolving the forces acting on a grain at its threshold of motion. Such models are based on parameters including grain size, grain protrusion relative to the surrounding bed topography, and grain pivot angle. These models are potentially valuable in quantifying bed mobility without the need for longer-timescale bed monitoring. However, the collection of grain-scale data required to parameterize these models has traditionally been difficult to employ over large areas or at multiple sites. Recent, novel applications of such grain force-balance models have used high resolution grain topography models and in situ bed resistance force testing (Feehan et al., 2023; Hodge et al., 2013; Prancevic & Lamb, 2015; Yager et al., 2018, 2024). These approaches have the potential to estimate in-channel τ_c^* distributions using fast and easily attainable field data, particularly given contemporary advances in portable, high resolution Structure-from-Motion (SfM) photogrammetry and LiDAR technologies (e.g. Smartphone LiDAR). If robust, these models would be a powerful tool in evaluating τ_c^* variability over wide spatial and temporal scales, for example, presenting an opportunity for large data set collection via citizen science. However, these force-balance approaches are largely theoretical, and have not been thoroughly tested on large sample sizes. Therefore, τ_c^* estimates derived from these methods have not been critically evaluated for consistency when applied to channel beds exhibiting notable differences in grain size, sorting and grain arrangements.

This study aims to quantify the interactions between grain arrangement and τ_c^* , employing two contrasting grain force-balance models to estimate bedload mobility threshold distributions for upland UK gravel-bed channels. To critically evaluate the usefulness and consistency of these models in assessing τ_c^* over regional scales, we outline two key objectives: (a) to estimate τ_c^* distributions derived from the two different models using in situ natural grain topographic data; and (b) to compare and critically evaluate a manual versus an automated approach toward estimating τ_c^* , presenting sensitivity analyses to test model assumptions, and accounting for differences and uncertainties in τ_c^* estimations between the two approaches. This work will provide a critical comparison of different force-balance model approaches, give an overview of their uncertainties, and potential applications in grain mobility research, using in situ natural field data.

2. Particle Entrainment Thresholds Theory

2.1. Grain Force-Balance Model

Dimensionless critical shear stress, τ_c^* , can be estimated at a grain-scale through the Kirchner et al. (1990) force-balance model by resolving forces acting on a single grain in both the vertical and horizontal directions (Figure 1a). Balancing the components acting on the target grain at its threshold of incipient motion reveals a force-balance expression outlined in Equation 1 (Wiberg & Smith, 1987).

$$\frac{F_D}{\tan(\varphi_{\text{piv}})} + F_L = F_W \quad (1)$$

This equation accounts for the grain pivot angle, φ_{piv} ; the angle through which the grain must rotate out of its resting position during the onset of particle transport. Expressions for each component force (drag, F_D ; lift, F_L and

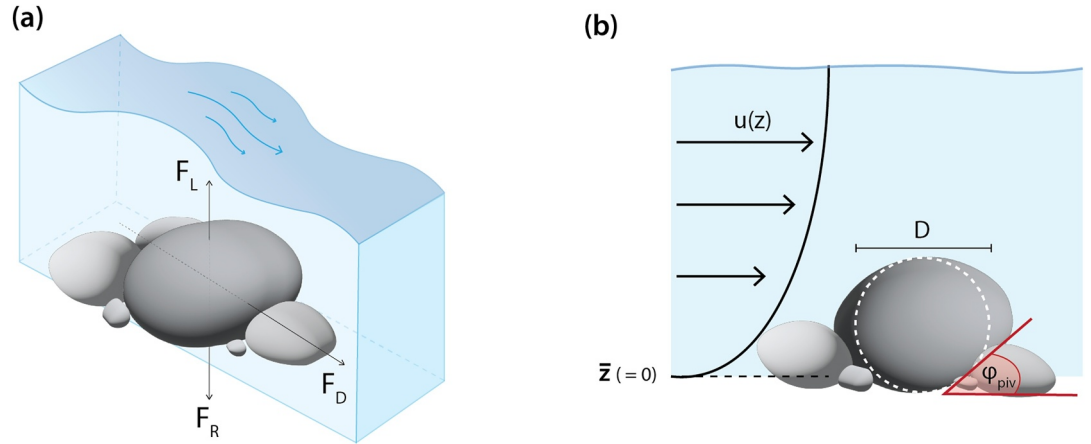


Figure 1. (a) Grain force-balance diagram for the Kirchner et al. (1990) model, illustrating that driving (lift, F_L and drag, F_D) forces and grain resistance force (F_R) are in balance at the threshold of grain motion. (b) Configuration of the logarithmic velocity profile, $u(z)$, used in the Kirchner model. In the force balance equations, particles are assumed to be spherical.

grain weight, F_w) are outlined in full in Kirchner et al. (1990). As part of these calculations, a logarithmic velocity profile (Figure 1b), is applied to the target grain, to describe the incident flow velocity, u , as a function of grain elevation, where $u(z) = 0$ at the local mean bed elevation, \bar{z} (defined here as $z = 0$):

$$u(z) = \sqrt{\frac{\bar{\tau}}{\rho}} \kappa^{-1} f(z)$$

$$f(z) = \ln\left(\frac{z + z_0}{z_0}\right) \text{ where } z > 0 \quad (2)$$

$$\text{and } f(z) = 0 \text{ where } z \leq 0$$

where bed roughness height, z_0 , is assumed as $0.1D_{84}$, and the von Karmen's constant, κ , is assumed as 0.4 (Hodge et al., 2013; Whiting & Dietrich, 1990). Grain protrusion (P) quantifies the grain maximum elevation relative to surrounding bed topography, and exposure (E) quantifies the height of the grain face which is exposed to flow (defined in detail in Section 3.5). Equations 1 and 2 are resolved and rearranged to estimate the forces on the grain at the point of entrainment, and thus τ_c :

$$\tau_c = 0.1(\rho_s - \rho)g \left(\frac{\pi D^3}{6}\right) \cdot \left\{ \frac{C_D}{\tan(\phi_{piv}) 2\kappa^2} \cdot \int_{P-E}^P \sqrt{D^2 - (2z - (2P - D))^2} f(z)^2 dz + \frac{\pi C_L D^2}{8\kappa^2} [f(P)^2 + f(P - D)^2] \right\}^{-1} \quad (3)$$

Equation 3 assumes that grains are spherical with diameter D , and as such, grain width, and therefore the exposed frontal area affected by the velocity profile, is calculated as a function of grain elevation z . Likewise, particle weight is approximated as a function of D , assuming that sediment density, $\rho_s = 2,650 \text{ kg m}^{-3}$, water density, $\rho = 1,000 \text{ kg m}^{-3}$ and gravitational acceleration, $g = 9.81 \text{ ms}^{-2}$ are constant for all grains. Grain pivot angle, ϕ_{piv} , can be calculated from in situ resistance force measurements (see Section 3.3). The drag and lift coefficients, C_L and C_D , are assumed to be 0.2 and 0.4 (Wiberg & Smith, 1987), respectively. Critical shear stress can then be expressed in its dimensionless form, τ_c^* , using:

$$\tau_c^* = \frac{\tau_c}{(\rho_s - \rho)gD} \quad (4)$$

2.2. Updated Kirchner Equations

An adapted version of the force-balance model is outlined in Yager et al. (2018), where the resistance force component, F_R , of the grain force-balance replaces $F_W \tan(\varphi_{\text{piv}})$ to also account for the influence of the partial burial of grains and intergranular friction (φ_{fric}). For submerged grains, F_R is expressed as the sum of the following resisting forces (detailed in Yager et al. (2024)):

$$\text{Grain Weight Component, } F_{\text{weight}} = \frac{g(\rho_s - \rho)\pi D^3}{6} \tan(\varphi_{\text{piv}}) \quad (5)$$

$$\text{Partial Burial Component, } F_{\text{burial}} = g(\rho_s - \rho)(1 - \lambda)V_0 \tan(\varphi_{\text{piv}}) \quad (6)$$

$$\text{Intergranular Friction Component, } F_{\text{friction}} = g(\rho_s - \rho)V_b \tan(\varphi_{\text{fric}})(1 - \lambda)C_v \quad (7)$$

where V_0 and V_b represent volumes of overlying sediment, and buried grain volume, respectively; assuming spherical grains, these variables can be calculated as a function of grain diameter and protrusion (see Yager et al., 2007, 2018). The volume correction factor ($C_v = 4.83$) and bed porosity ($\lambda = 0.6$) are assumed constant (Yager et al., 2018).

The adaptation of the Kirchner model utilized by Yager et al. (2024) incorporates an adapted velocity profile (Lamb et al., 2017), which is controlled by the bed roughness length, k_s (Equation 8):

$$f(z) = \ln\left(1 + \frac{30z}{k_s}\right) \quad (8)$$

Although z_0 is commonly assumed to be equal to $k_s/30$, and therefore k_s and z_0 are not interchangeable, the specific relation between k_s and grain size in this velocity profile equation is not well defined. To enable simplified comparisons between the two different force-balance models, we generally assumed that k_s also equaled $0.1D_{84}$, which could underestimate the roughness length in Equation 8. We later specifically explore the impact of k_s on the relative values of τ_c^* predicted from the two force-balance equations.

In both versions of the grain force-balance equations, lift and drag forces are calculated using assumed lift/drag coefficients, the exposed grain area to the flow, and the flow velocity acting on the particle. Equation 3 solves this force balance to determine the flow magnitude (i.e., τ_c) that is required to mobilize a given particle. Each sample, which exhibit combinations of grain sizes, resisting forces and topographies measured in the field, therefore contains a distribution of estimated flow magnitudes, and therefore τ_c^* , capable of mobilizing the grains within that sample.

2.3. Evaluating Novel Approaches for Estimating τ_c^*

In this study, we consider two novel applications of the Kirchner grain force-balance model, and apply each to a large data set of 45 UK gravel-beds to estimate τ_c^* . These methods have been developed and evaluated using a small number of field sites with limited variability. We compare the two approaches and evaluate the consistency in their estimated τ_c^* distributions for channel beds of varying grain size and sediment structure.

First, we explore a Monte Carlo style sampling approach outlined by Hodge et al. (2013); this approach utilizes the original Kirchner et al. (1990) equations, with inputs randomly sampled from distributions of manual grain measurements. The other method we consider is Pro+ (Yager et al., 2024); this approach uses automated measurements, derived directly from 3D bed topography models, using grains segmented by G3Point (Steer et al., 2022) to estimate τ_c^* for each identified grain in a sample area using the updated grain force-balance equations.

For each of the two approaches, we follow the workflows and definitions described in their original papers, Hodge et al. (2013) and Yager et al. (2024) respectively. Where appropriate, we make minor adaptations to sampling assumptions from the original papers to ensure that both approaches can be consistently applied to each of our large number of sites, and so that the inputs, equations and assumptions in each of the two approaches can be objectively compared and contrasted; for example, assuming that $k_s = z_0$.

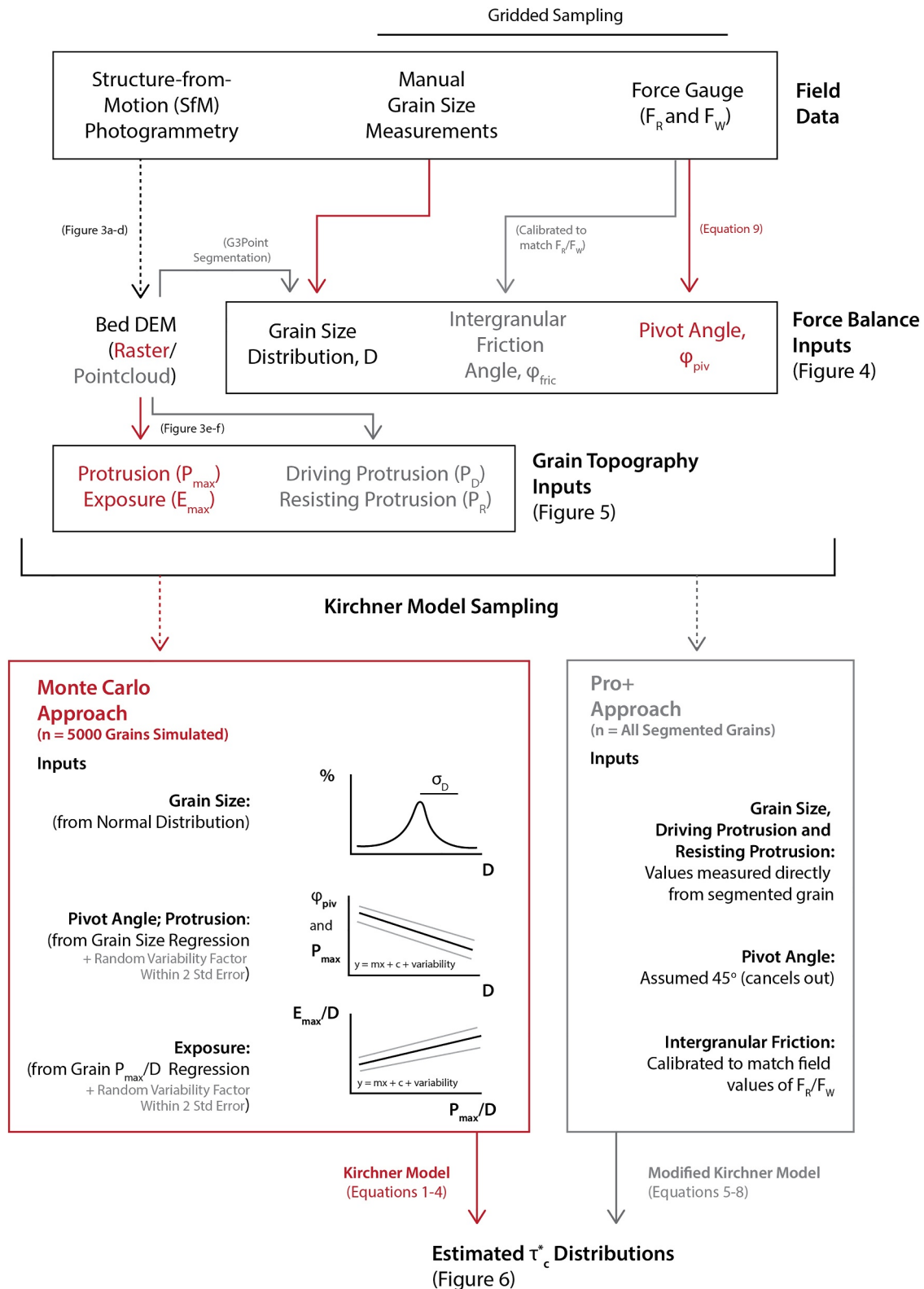


Figure 2. Workflows for estimating dimensionless critical shear stress from field data using both the Monte Carlo (red arrows) and Pro+ (gray arrows) approaches. The workflow for each approach is annotated, indicating the respective methods, assumptions and results outlined throughout the manuscript.

Each approach, and their respective methods and workflows, are outlined in Figure 2, and explained throughout Section 3. All differences in assumptions and force-balance equations between approaches are explicitly outlined throughout the manuscript, and their implications, as well as opportunities for further, more targeted, comparative analysis are further discussed in Section 5.

3. Methods

3.1. Field Locations

We investigated coarsely grained channel beds ($n = 45$) from 39 different upland gravel-bedded reaches across England and Wales (Table S1 in Supporting Information S1). Sampled gravel-beds exhibit a notable variability in Grain Size Distributions (GSDs), and microtopographies between sites (quantified in Section 4.1 and 4.3). All of the sites were located on gauged reaches; therefore, the hydrological regime and approximate flood history prior to sampling are known at each sample location.

Small ($\sim 1 \text{ m}^2$) patches of exposed channel bed were sampled (Figure 3a), with sample plots chosen to be broadly representative of surface grain sizes and grain arrangements across the local channel bed or exposed bar. Where there was prominent in-channel variability in bed material characteristics, multiple sample plots were identified as separate samples; for example, on steep bars where bed material characteristics varied with elevation up the bar, for example, River Conwy, Betws-y-Coed (Site S2a-b), or extensive gravel bars with in-bar features such as secondary channels, for example, River Duddon, Ulpha (Site C7a-b).

3.2. Structure From Motion Photogrammetry (SfM)

Grain-scale bed topography data was obtained via SfM photogrammetry at each plot (Eltner et al., 2015). For each SfM scan ($1 \times 1 \text{ m}$ dimensions), approximately 250–300 photographs were taken by a 12 Megapixel smartphone camera at various angles and distances. Images were processed, scaled and orientated via Pix4D. Generated 3D point cloud models were trimmed and de-noised using CloudCompare to remove statistical outliers (wherever point separation exceeded 1 standard deviation of mean point separation). Further details of the SfM photogrammetry approach, and systematic error analyses, are outlined in supplementary material; generally, SfM distances were within 1–2 mm of manually measured independent scale checks.

Point clouds were subsampled to 2 mm resolution, rasterized to produce digital elevation models (DEM), and linearly detrended, to be used for manual grain protrusion measurements (Figure 3b). G3Point grain segmentation and subsequent Pro+ analyses used topographic data in Point Cloud format (Figures 3c and 3d).

3.3. Particle Resistance Forces

In situ grain resistance forces, F_R , were measured in the field using a force gauge (Mecmesin BFG 1000: range = 1000 N, resolution = 0.2 N; error = $\pm 0.25\%$ of full scale). Force was applied to the center of the exposed grain face in the streamwise direction. F_R was recorded as the maximum force required to displace the target grain from a resting position by a distance of approximately half its diameter, that is, rotated completely out of its pocket. Grains ($n = 40\text{--}60$) were sampled systematically in a regular grid of spacing 150 mm (e.g., Figure 3b), beginning at the downstream side of the sample patch, to avoid disrupting grains upstream. Where multiple grid nodes fell on the same grain, the grain was sampled once.

Each tested particle was subsequently weighed (F_W). Resistance forces and grain weight measurements, F_R and F_W , respectively, were converted into pivot angle estimates using the conversion outlined in Johnston et al. (1998), where β is the local bed slope:

$$\tan(\varphi_p) = \frac{F_R - F_W \sin(\beta)}{F_W \cos(\beta)} \quad (9)$$

The local bed surfaces of our sampled channel beds were near-horizontal (generally $\beta \ll 0.01$), such that β had negligible impact on φ_{piv} . Local bed slope effects can therefore be neglected, and the pivot angle is assumed to be $\tan(\varphi_{\text{piv}}) \approx F_R/F_W$.

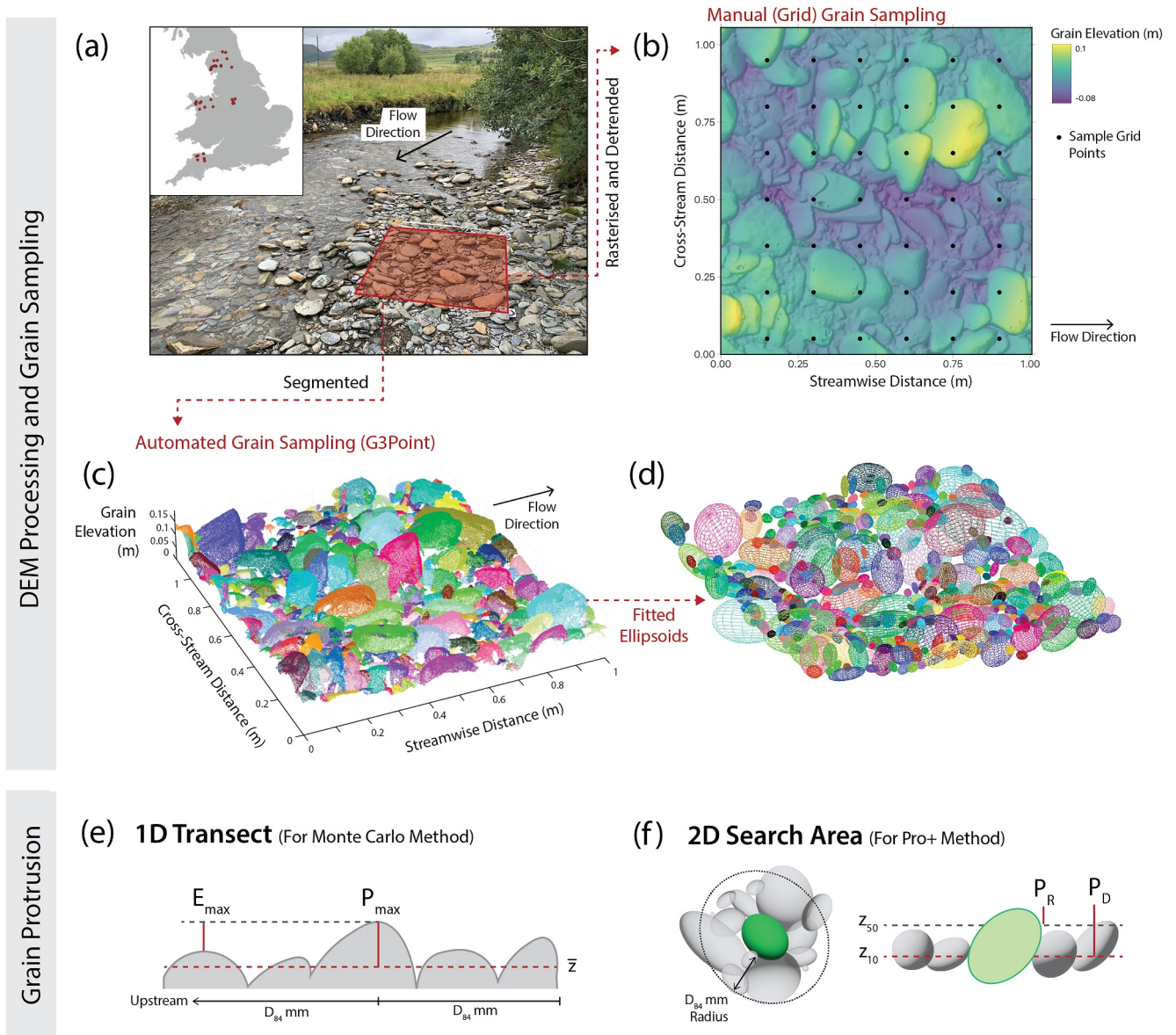


Figure 3. Grain sampling approaches: (a) Example of a Structure-from-Motion sample plot; surveyed gravel-bed patches are approximately 1 m^2 in area. Regional distributions of sample sites are shown as red points in the figure subplot. (b) Rasterized digital elevation models of the scanned gravel surface; black points indicate gridded sampling of manual grain protrusion and exposure measurements. (c) Gravel-bed pointcloud: points colored according to G3Point grain segmentation, and subsequently, (d) fitted grain ellipsoids. Protrusion definitions for Kirchner model inputs: (e) manual measurements over a 1D transect; protrusion (P_{\max}) is defined as elevation of the target grain maxima relative to local mean bed elevation, \bar{z} , and exposure (E_{\max}) is defined as the grain maxima elevation relative to the highest upstream elevation along the sampled transect. (f) Automated measurements within 2D search area surrounding target grain; driving protrusion (P_D) and resisting protrusion (P_R) are defined as the elevation of the target grain maxima relative to the 10th and 50th percentile elevations of surrounding grains respectively.

3.4. Grain Size Distributions (GSDs)

3.4.1. Manual Grain Measurements (Field)

The grain dimensions (a , b , and c axes) of each force tested particle were measured by caliper in the field. Grain size distributions were truncated for b -axis diameters $< 20 \text{ mm}$ to be consistent with the minimum discernible grain size in automated grain size measurements (Section 3.4.2).

3.4.2. Automated Grain Segmentation (G3Point)

GSDs were also generated automatically from point cloud data by segmenting the point cloud into individual grains via watershed segmentation using G3Point (Figure 3c). Oversegmented grains were merged and cleaned following the workflow outlined by Steer et al. (2022). This approach is sensitive to the G3Point segmentation input parameters (k , C_F , and α ; Steer et al., 2022), so these parameters were adjusted and cross-referenced with bed photographs and orthophotos until grain segmentation boundaries largely coincided with visually interpreted grain boundaries (Table S3 and Figure S1 in Supporting Information S1). Segmented grains were fitted with a reference ellipsoid (Figure 3d), and ellipsoid dimensions (abc -axis) were recorded for each identified grain. The minimum grain ellipsoid b-axis diameter for segmented grains was also set at 20 mm; we found this to be the minimum grain size to confidently discern grains from orthophotos for our photograph resolution. Two sites (PD4a and PD6a) were excluded from analyses on the basis of poor segmentation.

Note that this approach produced GSDs based on each grain in the sample (“area-by-number”) in contrast to the grid sampled GSD given by manual grain measurements, which is influenced by grain area coverage (“grid-by-number”). The latter GSD can theoretically be converted to account for biases introduced by area coverage (Bunte & Abt, 2001; Diplas & Fripp, 1992). In this study, we do not make this approximate conversion because the 1D grain protrusion measurements used in the Monte Carlo approach (Section 3.5) are also grid sampled, preferentially sampling protrusions of coarser particles; we therefore retain a consistent sampling bias across all Monte Carlo input measurements. The potential implications of using a grid-by-number versus area-by-number grain sampling on estimated τ_c^* distributions is discussed in Section 5.2.

3.5. Grain Topographies

3.5.1. 1D Protrusion Measurements

1D protrusion measurements, used in the Monte Carlo approach, were obtained for each sample DEM, which were grid sampled to select approximately 40–60 target grains (Figure 3b). Grid separation was held constant (150 mm) for each sample DEM to obtain a target of 40–60 sampled grains within the DEM area available; if two sample grid points fell on the same grain, it was measured just once. The maximum height of each sampled grain was identified from the DEM, and a 1D elevation transect was drawn upstream and downstream of the grain maximum, parallel to the presumed flow direction. Transect lengths were equivalent to the site D_{84} in each direction, and elevation values along each transect were 2 mm apart.

Grain Protrusion, P_{\max} , was defined as the maximum grain height, relative to the local mean bed elevation ($\bar{z} = 0$ mm) of the transect. Grain Exposure, E_{\max} , was defined as the maximum grain height relative to the maximum upstream elevation of surrounding grains along the transect (Figure 3e). These definitions are analogous to those used in Hodge et al. (2013), albeit with an adapted notation.

3.5.2. 2D Protrusion Measurements (Pro+)

Protrusion was also obtained automatically using Pro+ (Yager et al., 2024) for each grain segmented via G3Point. To quantify exposure to lifting forces, and the burial of a grain relative to its surrounding particles, a 2D search area of D_{84} mm radius from the segmented grain boundary was used to determine the protrusion relative to local surrounding bed topography (Figure 3f). Driving protrusion, P_D , was defined as the elevation difference between the grain maximum and the 10th percentile of grain elevations within the search area. Resisting protrusion, P_R , was defined as the elevation difference between the grain maximum and the 50th elevation within the search area (Yager et al., 2024).

3.6. Estimating τ_c^* Distributions

We used two documented approaches to estimate τ_c^* for each of the sampled patches: (a) a Monte Carlo style approach, which randomly sampled Kirchner force-balance model inputs from observed distributions of grain sizes, pivot angles, grain protrusions and grain exposures to calculate τ_c^* distributions at each patch; and (b) the Pro+ approach, which used data obtained directly from automatically segmented grains, along with updated Kirchner model equations, to estimate τ_c^* for each segmented grain in the sample. The former approach is useful when distributions of each parameter are sampled from a different selection of grains, whereas the latter approach utilizes a complete set of parameters for each grain in the sample.

For each approach, we followed the workflows outlined in the original papers, Hodge et al. (2013) and Yager et al. (2024), respectively, albeit with minor adjustments to the sampling to enable a more objective comparison between the two approaches and their respective methods for estimating τ_c^* , with our large data set. The two workflows we utilized are summarized below; a workflow summary for each method is outlined in Figure 2 for reference.

In both approaches, grains are assumed to be spherical. In reality, sampled beds comprised grains of varying shapes, including sub-spherical, angular and flat clasts. These grain shape effects, and associated uncertainty in estimated τ_c^* , are not directly incorporated into the force balance equations. However, grain shape effects are indirectly incorporated into τ_c^* estimates, as they affect bed resistance force, pivot angle and protrusion measurements. For example, flatter grains theoretically exhibit lower protrusions relative to their diameter, and low protrusions yield systematically higher F_R (Yager et al., 2018).

3.6.1. Monte Carlo Sampling

We first employed a Monte Carlo style sampling approach, analogous to that outlined by Hodge et al. (2013), to estimate critical shear stress distributions at each site. Grain sizes of simulated grains were sampled randomly from an assumed normal distribution within 1 standard deviation of the measured site D_{50} (e.g., Figures 4a and 4b); the effect of this assumption on the resulting distribution of τ_c^* is quantitatively tested in Supporting Information S1. For each sample patch, the grain pivot angle and protrusion inputs were both sampled from their grain size regression line fit to the field data at each site \pm a variability factor (e.g., Figure 5b), where the additional variability factor was randomly sampled within 2 standard errors of the regression. Finally, grain exposure inputs are sampled from a regression between dimensionless grain protrusion, P_{\max}/D , and dimensionless grain exposure, E_{\max}/D , measured in the 1D grain topography analyses \pm the variability factor (e.g., Figure 5c). Inputs for each sample site are listed in Tables S4–S6 in Supporting Information S1.

For each site, each parameter was randomly sampled for $n = 5,000$ simulated grains. In this approach, τ_c^* is then calculated using the Kirchner force-balance model outlined in Section 2.1, Equations 1–4.

3.6.2. Pro+ Sampling

Conversely, in the Pro+ approach (Yager et al., 2024), τ_c^* estimates are provided for each segmented grain in the 1 m^2 sample area, using automated grain size and protrusion (P_R and P_D) measurements obtained directly from the point cloud. In this approach, we assumed that the pivot angle is 45° for each grain to avoid having to assume a certain pivot angle distribution, which can contain uncertainties (see Yager et al., 2024). Instead, we incorporate the grain resistance force into the τ_c^* calculation by adjusting the intergranular friction angle (ϕ_{fric}). We adjusted ϕ_{fric} in 10° increments until the median modeled F_R/F_W value generated by Pro+ closely matched the median F_R/F_W from field measurements at each site (Figure S2 in Supporting Information S1). The selected ϕ_{fric} value was assumed to be constant for all segmented grains in each sample. In this approach, τ_c^* is calculated using the updated Kirchner force-balance model and velocity profile outlined in Section 2.2, Equations 5–8.

We performed additional sensitivity analysis for an example site (River Duddon, Site C6a) to evaluate the sensitivity of the Pro+ τ_c^* estimates to the assumed ϕ_{fric} and k_s values employed in the main analyses. This included an investigation into the influence of adding different degrees of variability to the assumed ϕ_{fric} between each grain within the sample.

4. Results

4.1. Grain Size Distributions

Grain sizes measured manually were coarser (median = 75 mm; IQR = 45 mm) than segmented grain ellipsoid dimensions (median = 36 mm; IQR = 26 mm) across the entire sample (Figure 4a). Median b -axis, D_{50} , at each site ranged from 43 to 110 mm in the manual approach, and 31–50 mm in the automated approach. Note that in each case, GSDs were truncated at a minimum diameter of 20 mm. Grain size data are available in Table S4 in Supporting Information S1.

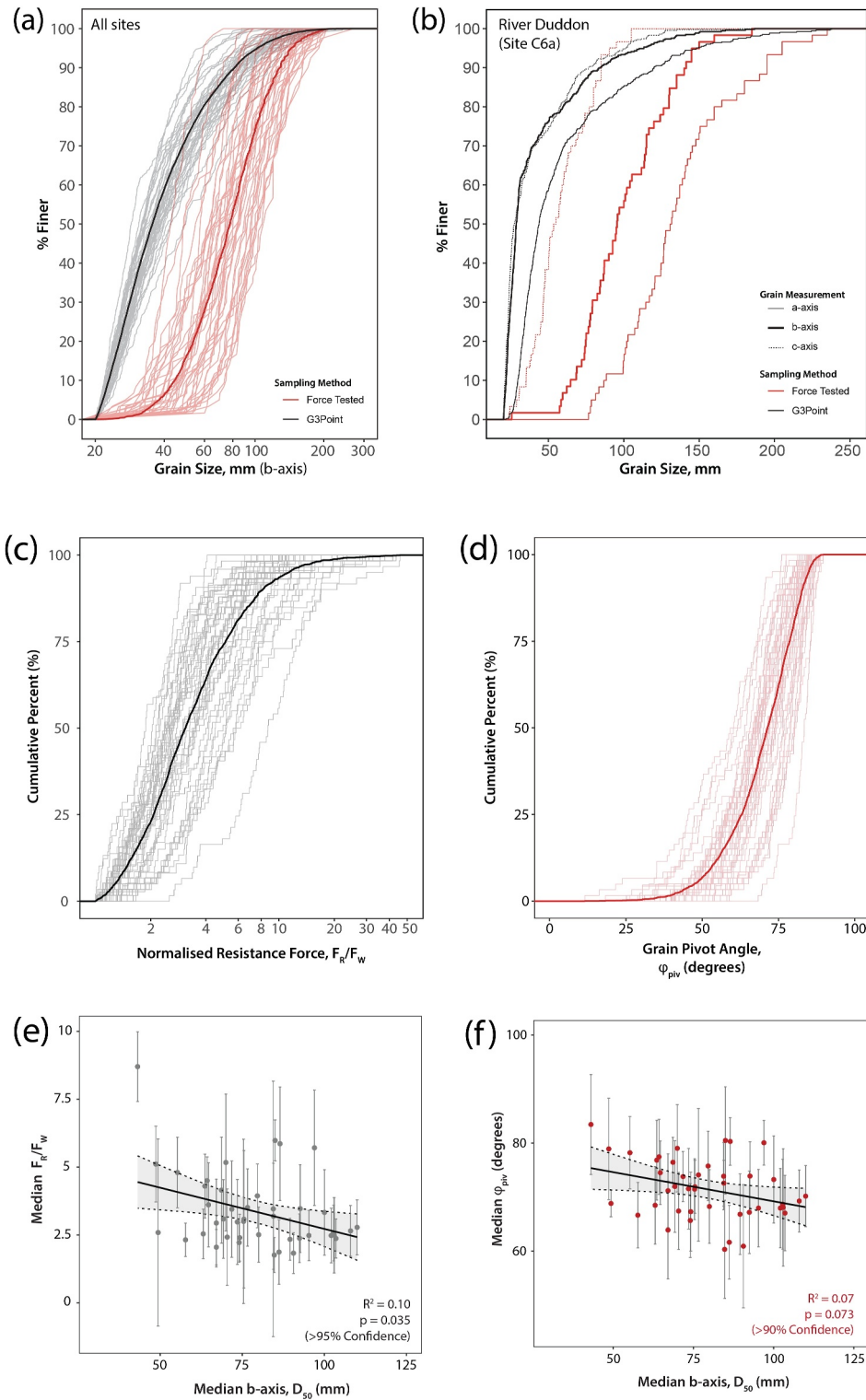


Figure 4. (a) Grain size (*b*-axis) distributions for all sample sites ($n = 45$); manual grain size measurements (of force tested grains) are shown in red, and grain size measurements determined from G3Point ellipsoids (of automatically segmented grains) are shown in black. Darker lines illustrate the combined Grain Size Distributions (GSDs) for each method across all sites. (b) A comparison of GSDs (*a*, *b*, and *c* axes) for each approach, at a single sample site; River Duddon, Cumbria. (c) Cumulative distributions of normalized resistance force (F_R/F_W) measured at each site; combined F_R/F_W distributions for all sites are illustrated by the darker black line. (d) Cumulative distributions of grain pivot angles, φ_{piv} , calculated from force gauge measurements via Equation 9; combined φ_{piv} distributions for all sites are illustrated by the darker red line. (e–f) Influence of median grain size, D_{50} , on median F_R/F_W and φ_{piv} respectively. Shaded gray region indicates the 95% confidence limits of the regression. Error bar length is equal to the interquartile range for each site.

GSDs for each recorded grain axis are also outlined for a single sample location (River Duddon, Cumbria; Site C6a) in Figure 4b. Median *a/b/c* axes for manual measurements (131, 95, 54 mm, respectively) were systematically coarser than segmented ellipsoids (44, 29, 24 mm, respectively).

4.2. Particle Resistance Force

4.2.1. Normalized Resistance Force

F_R/F_W values (the force required to initiate bed material transport normalized by its grain weight) were notably variable between sites (Figure 4c); median measured F_R/F_W for individual sample locations ranged from 1.8 to 8.7. Across all sample sites, the median F_R/F_W was 3.0 (IQR = 3.0, $n = 2,921$ grains). There is a weak grain size relation where F_R/F_W generally decreases for coarser grain sizes (Figure 4e; $p < 0.05$). Grain force-balance data for each site are summarized in Table S5 in Supporting Information S1.

4.2.2. Pivot Angle

The median estimated pivot angle, φ_{piv} varied from 60° to 83° between sites (Figure 4d), where median φ_{piv} across the entire sample measured 71° (IQR = 16°). Median pivot angle for each site also decreased subtly with increasing site D_{50} (Figure 4f; $p < 0.1$).

4.2.3. Intergranular Friction Angle

Adjusted intergranular friction angles, φ_{fric} , varied from 20° to 70°; these angles were identified such that Pro+ predictions of median F_R/F_W aligned with median F_R/F_W measured in the field (Figure S2a in Supporting Information S1). Note that F_R/F_W values estimated by Pro+ generally followed a similar distribution to field measurements for the lower 50th percentile of the F_R/F_W distribution, but eventually reached an upper threshold at approximately the 50th percentile, indicating a maximum possible F_R/F_W value, which systematically increases for higher assumed φ_{fric} angles. In contrast, field F_R/F_W distributions continued to increase, and are particularly influenced by very immobile grains. Calibrated φ_{fric} increased with median F_R/F_W and φ_{piv} at each sample location (Figures S2b and S2c in Supporting Information S1 respectively).

4.3. Grain Topographies

4.3.1. 1D Protrusion Measurements

Grain protrusion and exposure from the 1D grain transect analysis, P_{max} and E_{max} , respectively, systematically increased with coarsening grain sizes (Figures 5a–5c). This trend was observed across regional scales (Figure 5a) and within individual survey patches (Example site: River Duddon, C6a; Figure 5b). Median P_{max} was generally on the order of 50–100 mm higher elevation than median E_{max} at each site; median P_{max} ranged from 40 to 230 mm, whereas median E_{max} was notably more variable, ranging from –5 (i.e., entirely unexposed) to 210 mm.

Dimensionless expressions of grain protrusion and exposure, P_{max}/D and E_{max}/D are plotted against each other in Figure 5c for the single example site; this reveals a systematic increase in normalized grain exposure with increasing grain protrusion ($R^2 = 0.60$; $p < 0.001$). Note that although P_{max}/D and E_{max}/D are normalized by grain size, a grain size signal remains, where coarser grain sizes yield larger P_{max}/D and E_{max}/D values (Figures S3a and S3c in Supporting Information S1), albeit with low significance; $R^2 = 0.12$ and 0.20 respectively.

4.3.2. 2D Protrusion Measurements (Pro+)

Automated 2D protrusion measurements reveal similar grain size relations to the manual measurements (Figures 5d–5f). For each grain identified in the site C6a sample (Figure 5e), P_D and P_R systematically increased with increasing ellipsoid diameter. Likewise, across all sites, median P_D increased with particle diameter. In contrast, median P_R was relatively insensitive to grain size (Figure 5d). Finally, normalized driving protrusion (P_D/D) and normalized resisting protrusion (P_R/D) were correlated ($R^2 = 0.45$; $p < 0.001$) (Figure 5f).

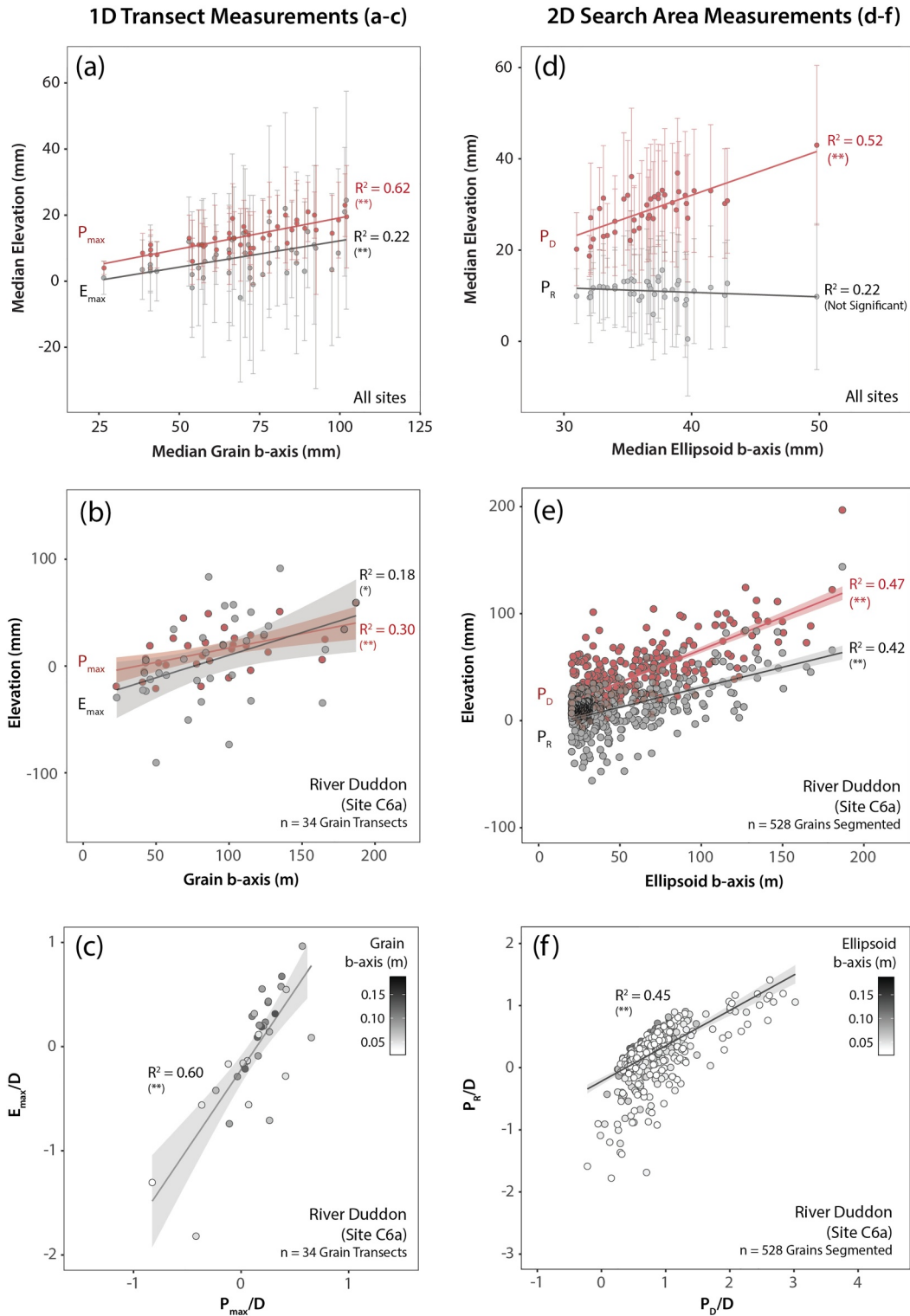


Figure 5. Grain protrusion measurements for the manual (a–c) and automated (d–f) approaches are outlined in Figure 3. (a) Influence of grain size on median grain protrusion, P_{max} , and exposure, E_{max} , across all sampled field sites. Error bar length is equal to the interquartile range for each site. (b) Influence of grain size on P_{max} and E_{max} for each sampled grain at the River Duddon site, Cumbria. (c) Normalized grain protrusion P_{max}/D versus normalized grain exposure E_{max}/D for each sampled grain at the River Duddon site, Cumbria. Subplots (d–f) highlight the same relations, instead using the automated grain topography definitions illustrated in Figure 3; driving protrusion, P_D and resisting protrusion, P_R . Highlighted gray and red regions indicate 95% confidence limits. Pearson's correlation confidence limits are annotated for each regression, where (*) = $p \leq 0.05$ (95%); and (**) = $p \leq 0.001$ (99.9%). Regressions shown in subplots b and c are used as inputs for the Monte Carlo modeling for the Duddon River site. Regressions in subplots e and f are for comparison only; in practice, these relationships are nonlinear.

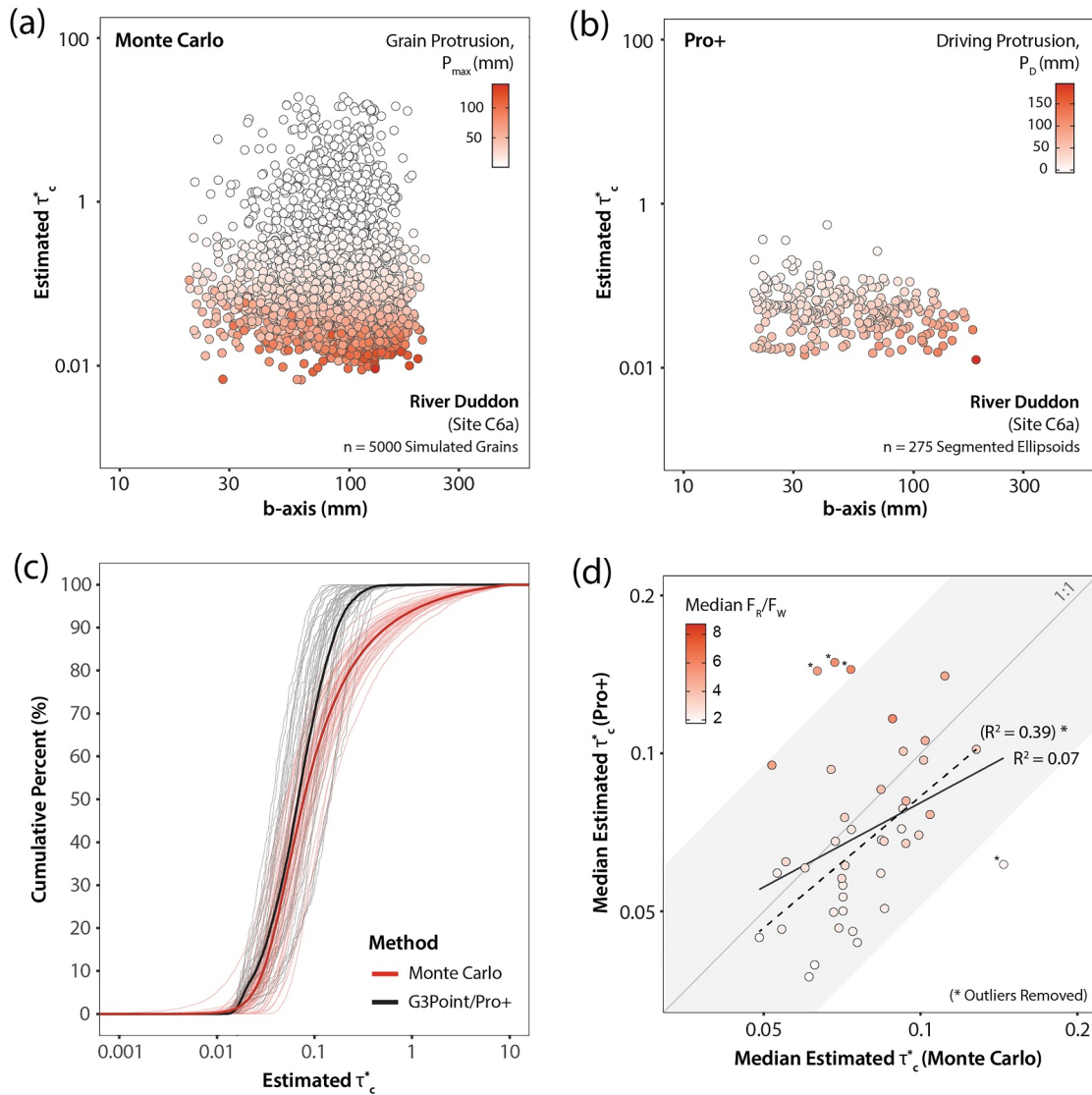


Figure 6. Estimated dimensionless critical shear stress, τ_c^* for (a) each simulated grain in the Monte Carlo sampling approach, and (b) each segmented grain in the Pro+ approach. Points are colored by the protrusion of the sampled grain in each approach; P_{max} and P_D respectively. (c) Cumulative distribution of τ_c^* for both the Monte Carlo (red) and Pro+ (black) approach; darker line indicates the combined τ_c^* for all grains sampled across all sites. (d) Comparison of median dimensionless critical shear stress (τ_c^*) estimated by the Monte Carlo and Pro+ approaches at each site; points are colored by the median measured excess force, F_R/F_W , at each site. Four outlier sites (*) are also identified and removed from correlation analysis; these are points which deviate from the 1:1 line greater than 2x the standard error of the regression (gray area).

4.4. Estimated Bed Mobility Thresholds (τ_c^*)

4.4.1. Monte Carlo Sampling

At the River Duddon (C6a) site, τ_c^* estimates ranged from 2.80×10^{-4} to 19.1 (median $\tau_c^* = 0.068$, IQR = 0.121) for $n = 5,000$ simulated grains of diameters ranging 20–210 mm (Figure 6a). For any given grain size, more protruded grains yielded the lowest τ_c^* estimates, with an abrupt threshold at around $\tau_c^* \approx 0.010$, below which very few τ_c^* estimates occurred; this marks the likely minimum threshold for τ_c^* for the sample. In contrast, the least protruded grains exhibited high τ_c^* estimates. There was no obvious maximum threshold for bed mobility estimates. τ_c^* distributions show a weak but significant correlation with grain size; scatter between individual points results in no obvious visual trend (Figure 6a, $R^2 = 0.002$; $p < 0.01$).

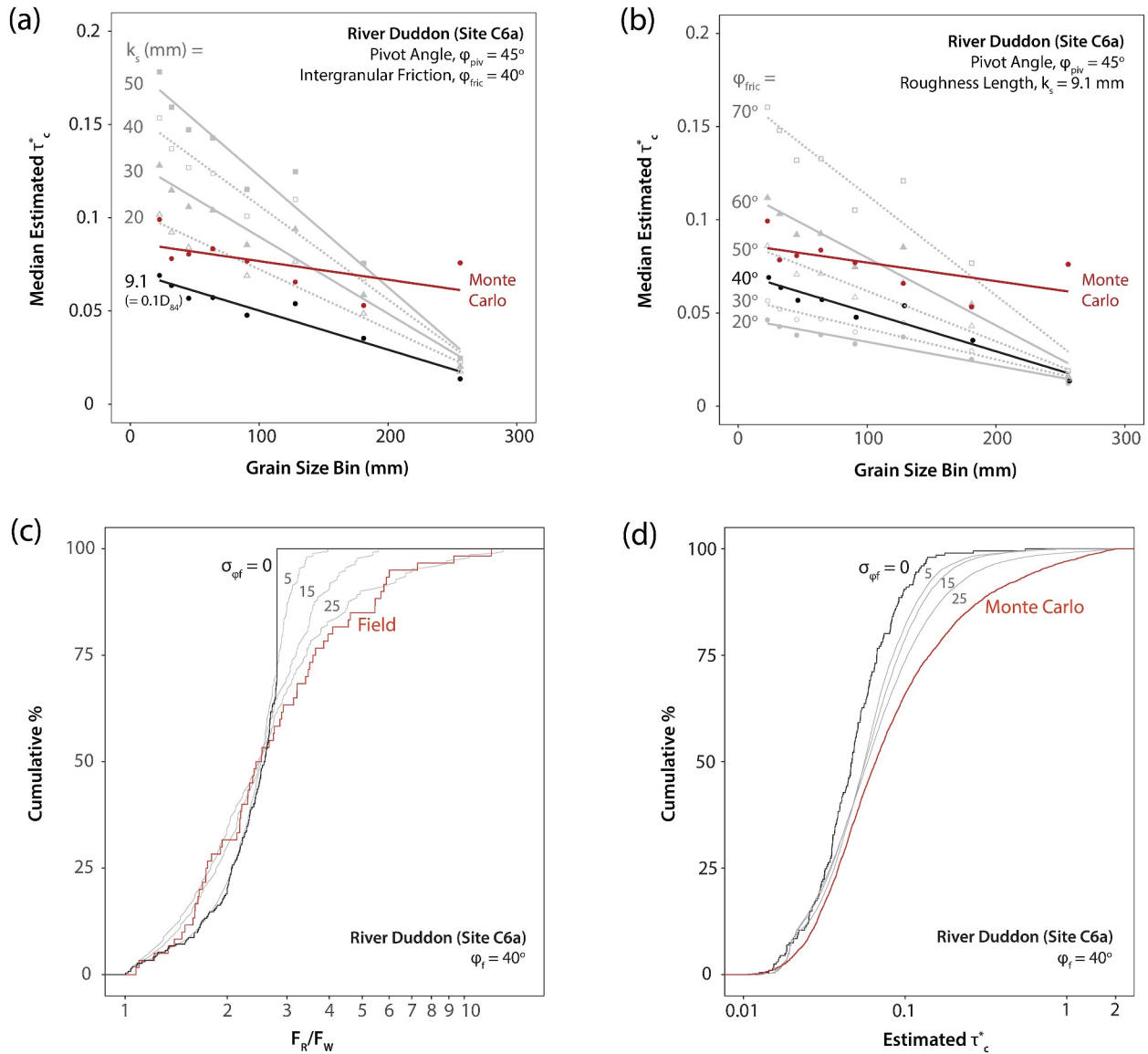


Figure 7. Sensitivity of estimated τ_c^* to (a) bed roughness length, k_s , and (b) intergranular friction angle ϕ_{fric} , in the Pro+ model at the River Duddon site. τ_c^* distributions are binned by grain size in $1/2$ phi scale, and represented as a median, τ_c^* estimate for each grain size bin. Black points indicate k_s and ϕ_{fric} conditions used in the Pro+ approach employed throughout this study. Red points indicate the grain-size binned τ_c^* estimates Monte Carlo for the same sample site for comparison. (c–d) Influence of adding an intergranular friction angle variability, $\sigma_{\phi f}$, into the Pro+ model on panel (c) F_R/F_W distribution and (d) τ_c^* distributions. For reference, in (c) the red line shows field measurements, and in panel (d) the red line outlines results generated by the Monte Carlo style approach, which incorporates a randomly sampled pivot angle into the Kirchner model calculation.

4.4.2. Pro+

For the same River Duddon (C6a) sample, bed mobility estimates derived from the Pro+ approach were less variable (Figure 6b), ranging from 0.013 to 0.554 (median $\tau_c^* = 0.050$, IQR = 0.039) for $n = 275$ segmented grains. τ_c^* estimates show no correlation with grain size (Figure 6b, $R^2 = 0.04$; $p < 0.01$), but were higher for grains which exhibited low driving protrusions. Grain-size binned τ_c^* distributions reveal a systematic decrease in median τ_c^* with increasing grain size (Figure 7).

4.4.3. Comparison of τ_c^* Distributions

τ_c^* distributions for the Monte Carlo and Pro+ approaches for all patches were largely consistent below the median estimated τ_c^* values (Figure 6c; Table S7 in Supporting Information S1). In contrast, in the 70th to 100th

percentiles of the distribution curves, τ_c^* estimated using the Monte Carlo approach was systematically higher than that estimated by Pro+. Median τ_c^* at each site ranged from 0.05 to 0.14 in the Monte Carlo approach and 0.04 to 0.15 in the Pro+ approach. The median estimated τ_c^* for each approach was largely consistent across all sites, excluding four identified outliers (Sites E2a, E8a, YP1a, and YP2a), which each deviated from the 1:1 line by a value greater than two times the standard error of the regression containing all site data (Figure 6d; $R^2 = 0.39$). In Figure 6d, points are colored by median measured F_R/F_W , which demonstrated a notably stronger influence on median estimated τ_c^* in the Pro+ approach in comparison to the Monte Carlo approach, for example, exhibiting a more apparent color gradient on the y-axis versus the x-axis (see also Figure S4 in Supporting Information S1).

4.5. Sensitivity Analysis of Pro+ Inputs

The sensitivity of Pro+ τ_c^* estimates to the assumed input parameters (roughness length, k_s , and intergranular friction angle, φ_{fric}), with respect to particle grain size, are demonstrated in Figures 7a and 7b, respectively, for the example site C6a. Median τ_c^* from each grain size bin was systematically reduced with decreasing k_s and φ_{fric} . In both cases, τ_c^* estimated using our assumed Pro+ input parameters (black points) was sensitive to grain size. For larger values of assumed k_s and φ_{fric} , this observed grain size sensitivity became more notable.

The sensitivity of Pro+ τ_c^* estimates to variability in intergranular friction angle is also explored in Figures 7c and 7d, for the example River Duddon site C6a. Instead of using a constant value, incorporating a standard deviation value, σ_{φ_f} allowed Pro+ to sample the intergranular friction angle from a range of values to generate a range of τ_c^* for each grain. Adjusting σ_{φ_f} in increments of 10° influenced the F_R/F_W distribution curve (Figure 7c), resulting in systematically increased F_R/F_W values in the ~ 70 – 100 th percentile, and reduced F_R/F_W values in the lower ~ 30 th percentile. At this sample site, F_R/F_W distributions calculated by Pro+ became more consistent with F_R/F_W distributions measured directly in the field (force gauge) with increased σ_{φ_f} . Consequently, in this example, larger σ_{φ_f} values ($>25^\circ$) resulted in τ_c^* distributions more consistent with those generated by the Monte Carlo sampling approach; this is particularly prominent for upper 50th percentile τ_c^* values in the estimated distribution curve.

5. Discussion

5.1. Comparison of τ_c^* Estimates

The Monte Carlo approach employed in this study yields a broader range of τ_c^* values, and systematically greater median τ_c^* for each sample than our application of Pro+ (Figure 6). The Monte Carlo-derived distributions for the example site documented in Figures 6a and 6b also exhibit a considerable proportion of high τ_c^* values (e.g. $\tau_c^* > 1$), in contrast to the Pro+ distributions at the same site, which does not estimate any τ_c^* values exceeding ~ 1 . However, the Pro+ and Monte Carlo approaches yield similar τ_c^* distributions for the lower end of their τ_c^* distribution curves; this is important to note because the lower values of τ_c^* are most relevant when interpreting the onset of sediment transport.

We deduce that the difference in τ_c^* distribution ranges is largely a result of the differences in the way in which parameter values are combined between approaches. In the Monte Carlo approach, Kirchner force-balance model inputs are randomly sampled from normal distributions fitted to field data. We anticipate that high τ_c^* estimates arise when unrealistic combinations of inputs are sampled. For example, in the River Duddon Site (C6a), very low grain protrusions, $P_{\text{max}} < 5$ mm, combined with very high grain pivot angles, $\varphi_{\text{piv.}} > 80^\circ$ result in high τ_c^* , ranging from 1 to 20; whilst these combinations could represent the infrequent occurrence of buried grains, clasts exhibiting these extreme combinations were not generally observed in the field. In contrast, Pro+ distributions likely yield a much narrower range of τ_c^* values, because the combination of parameters for any individual grain is directly measured rather than sampled from distributions. But, we also assume that the intergranular friction angle and the pivot angle are the same for every grain in the Pro+ sample; we further explore intergranular friction variability and its influence on Pro+ derived τ_c^* distributions in Section 5.2.4.

5.2. Key Sources of Uncertainty

Through our comparison of estimated dimensionless critical shear stress values for the Monte Carlo style, and automated Pro+ approach, across each of our 45 field sites, we identify key uncertainties leading to discrepancies

between the two approaches. These uncertainties are explored here, particularly drawing on exceptions (e.g., the four identified outlier sites identified in Figure 6d), which reflect inconsistencies between the tested approaches.

5.2.1. Grain Size Biases

Contrasting grain sampling approaches employed by the manual and automated methods result in marked differences in the resulting GSDs illustrated in Figure 4a. Automated grain segmentation provided by G3Point point cloud analysis yields a systematically finer grain size than manual (physically measured in the field) GSDs. We attribute this largely to the differences in sampling techniques. Automated measurements were taken as a bulk GSD for every grain segmented in the sample (area-by-number), whereas manual measurements were grid-sampled, and therefore biased toward sampling larger material with greater planform surface area (grid-by-number) (Di Francesco et al., 2016; Graham et al., 2012). We acknowledge that manually sampled GSDs can be converted to account for area coverage sampling bias (Bunte & Abt, 2001; Diplas & Fripp, 1992; Graham et al., 2012). We did not make this conversion in our comparisons because the same sampling biases are present across all manual (grid-sampled) measurements. Furthermore, grain size conversions incorporate additional uncertainties, and there is little documented evidence to support which of the grain size sampling approaches offer a GSD that is most representative of the “true” GSD of the sampled bed. Conversely, it would be possible to convert area-by-number outputs from G3Point to grid-by-number for use as Pro+ GSD inputs by using a digital resampling grid on the segmented point cloud (Mair et al., 2024; Steer et al., 2022). This would improve comparability in GSDs between both approaches without introducing additional uncertainty, but would forfeit having concurrent grain size and protrusion data for each segmented grain in the sample, and underrepresent finer grain size fractions, which are the main advantages of using Pro+ over the Monte Carlo approach.

5.2.2. Automated Grain Segmentation

An additional source of uncertainty in the automated GSDs is the G3Point grain segmentation (e.g., Figure S1 in Supporting Information S1). We utilized visual checks (cross-referencing segmentation boundaries with field photographs and orthophoto; e.g. Butler et al., 2001; Steer et al., 2022) to fine-tune the success of the G3Point grain segmentation, we identified recurrent situations in which the grain segmentation quality was compromised. Most notably, the presence of tabular or flat imbricated clasts generally resulted in grain under-segmentation because the angle between the two grains, at the grain boundary, is reduced. This under-segmentation can be addressed by adjusting the minimum threshold angle that defines two separate grains; however, for samples where grain size and imbrication extent are not spatially consistent, this often leads to over-segmentation of remaining grains within the sample. Likewise, over-segmentation generally occurs in samples with larger angular and irregular cobbles (Butler et al., 2001; Sime & Ferguson, 2003). We therefore find that G3Point segmentation is most effective for rounded and well sorted samples.

In future applications of G3Point, we suggest performing an additional check of the grain segmentation by measuring the GSD for the entire sample, and altering G3Point segmentation parameters until the GSD of G3Point segmented grains align with those noted from the true GSD (see Yager et al., 2024). This additional test will still require a detailed visual check of grain boundaries, as undersegmentation and oversegmentation may balance each other out to produce a GSD that is consistent with field data but using misidentified grains. Machine learning and photo sieving approaches could also be utilized for improved automatic identification of grain boundaries (Butler et al., 2001; Graham et al., 2005; Mair et al., 2024) or the SegmentEveryGrain tool.

Even with thorough validation of the grain segmentation, all photogrammetry and grain segmentation techniques likely underestimate grain size to some extent due to partial burial of grains (Garefalakis et al., 2023). To address the influence of this uncertainty, partial burial of grains can be quantified in the field by dyeing the exposed planform area of the clast, and evaluating the proportion of exposed versus covered parts of the target grain (Sanguinito & Johnson, 2012). Likewise, grains with a vertical or near-vertically orientated b-axis are also likely underestimated.

Grain size-derived uncertainties, both via segmentation error and sampling bias, are not consistent across all sites. It is therefore difficult to evaluate their relative influence on estimated τ_c^* . We find that median τ_c^* decreases for coarser grain size fractions (Figure 7); therefore, these grain size uncertainties are worth considering as they will have some influence on estimated grain mobility thresholds.

5.2.3. Defining Protrusion

Differences in the definition and incorporation of grain protrusion and exposure into the force-balance models also contribute to differences in τ_c^* distributions for each approach. Whilst grain protrusion measurements, which influence grain driving force, are not directly comparable between the 1D transect (P_{\max}) and 2D search radius (P_D) approaches, as they are defined relative to mean and tenth percentile local bed elevation, respectively, they play essentially the same role in the force-balance models.

P_{\max} measured from 1D transects is generally notably lower than anticipated. We expect that this is because we define the local mean bed elevation for each 1D transect across a given distance, D_{84} , from the grain maximum. Much of the sampled grain itself is therefore included in the mean bed elevation; this is particularly notable for flat, well imbricated clasts (e.g., Afon Colwyn, Site S5a). This could be mitigated by beginning the 1D transect from the grain boundary rather than the grain maxima (Buffington et al., 1992; Hodge et al., 2013; Smith et al., 2023), but requires reliably defined grain boundaries; these can be drawn manually but are sometimes subjective and time consuming, especially for large sample sizes such as those used in our study.

P_D values were notably higher than P_{\max} values because it is defined from a lower reference elevation. The large difference between P_D and P_{\max} is also likely exacerbated by the underestimation of P_{\max} outlined above. This may account, in part, for higher-than-expected τ_c^* distributions in the Monte Carlo approach versus Pro+, particularly for higher percentiles of τ_c^* . In future studies, for manual protrusion measurements, we therefore recommend manually digitizing sampled grain boundaries and removing the target grain from mean bed elevation calculations (e.g., Hodge et al., 2013); for sample sizes as large as that employed in our study, this was unfeasible, and therefore reinforces the benefit of automated tools such as Pro+ for fast acquisition of protrusion measurements across large samples.

5.2.4. Representing Resistance Force

Resistance force, F_R , is accounted for in the Monte Carlo approach via pivot angle, φ_{piv} , sampled from measured trends with grain size across each sample, and in the Pro+ approach via calibrated intergranular friction angle, φ_{fric} , assumed constant for each sample, to match median F_R/F_W measurements. Given that our calibrated φ_{fric} is assumed constant for each grain, our Pro+ τ_c^* estimates exhibited less variation in F_R than they would if φ_{fric} was allowed to vary. Consequently, we find that estimated τ_c^* at each patch is therefore sensitive to the median F_R/F_W measured within the patch (Figure 6d). Grain size binned sensitivity analysis in Figure 7b reveals that a 10° increase in φ_{fric} results in a large (up to +0.05; approximately 30% increase) change in median τ_c^* for smaller grain sizes, where grains were binned by their b axis length in $1/2$ phi scale. The relative influence of altering φ_{fric} on estimated τ_c^* systematically reduces for larger grain sizes. τ_c^* becomes less size-selective as the intergranular friction angle increases, indicating a strengthening of the hiding effect with increasing φ_{fric} . The same applies for altering the roughness length k_s (Figure 7a; Section 5.2.5). These are important observations for Pro+ users when assessing the relative mobility of different grain sizes because altering φ_{fric} (and k_s) does not result in systematic changes in particle mobility for all grain size fractions.

Anomalously high Pro+ τ_c^* estimates for outlier sites E8a, YP1a, and YP2a, each of which have an assumed φ_{fric} of 70° , are likely due to particularly high F_R/F_W inputs. High F_R/F_W values at these sites are corroborated by field evidence; for example, site E8a contained a high density of clays and plant roots underneath the mobile layer, which likely provides additional grain cohesion (Barzilai et al., 2013; Caponi & Siviglia, 2018).

Adding an intergranular friction angle variability (σ_{φ}) reduces the observed discrepancy between estimated Pro+ and Monte Carlo τ_c^* distributions for the most immobile grains, for example, 70th to 100th percentiles (Figures 7c and 7d). Note that this is how Pro+ was initially designed to function, essentially incorporating a Monte Carlo style φ_{fric} approach such that modeled F_R/F_W distributions align more closely to those observed in the field. For the main comparison of approaches, we did not incorporate this φ_{fric} variability into our application of Pro+ to avoid subjectivity across different samples. We advise that future applications investigate this further to develop a consistent method for identifying the optimal combination of inputs (φ_{fric} and σ_{φ}) needed to match modeled F_R/F_W distributions to those measured in the field with some level of statistical confidence.

The F_R measurements collected via the force gauge are also associated with sampling uncertainties. Measured F_R is sensitive to field approaches, such as subtle differences in the rate of application of the load, and the section of the grain that the load is applied to. We recommend that all F_R measurements collected across the entire sample of

a study be conducted by the same person to maintain consistency between samples. Alternatively, since protrusion is shown to be a principal driver of τ_c^* (Yager et al., 2018), in the case that there are no F_R measurements, then the φ_{fric} value could be assumed for a given site; consequently, τ_c^* will be only locally informed by the grain microtopography within the sample. In this case, our mean calibrated φ_{fric} across all sample sites, of approximately 50° , is a useful guide to inform assumed φ_{fric} values in the absence of force gauge data.

5.2.5. Assumed Bed Roughness Length

In our Pro+ analyses, we assume that the roughness length (k_s) is equal to $0.1D_{84}$. This assumption was made to be consistent with the roughness height used in the Monte Carlo approach to simplify comparisons. In other literatures, k_s is often assumed to be D_{84} or $2D_{84}$ (e.g., Church et al., 1998; Qin & Ng, 2012; Qin et al., 2019). In the sensitivity analysis (Figure 7a), we find that small changes in k_s can have considerable influence on estimated τ_c^* , where increasing k_s from $0.1D_{84}$ to $0.5D_{84}$ resulted in an almost 3x increase (0.05–0.15) in τ_c^* for grains <32 mm. This is also grain size dependent, where coarser grains exhibit a systematically lower increase in τ_c^* as k_s increases; choosing a reliable k_s is therefore important but difficult in samples with differing degrees of sorting.

5.3. Applications of Grain Force-Balance Models

The presented grain force-balance models show potential to be powerful tools in river channel management, sediment transport research and wider geomorphology applications. In applied contexts, sediment transport thresholds estimated via force-balance models can be useful in predicting the flux and accumulation of material throughout catchments (Chapman et al., 2021; Pfeiffer et al., 2017; Slater et al., 2015, 2019). The median τ_c^* estimates derived from the force-balance methods investigated in this study (ranging approximately from 0.05 to 0.15 between sites) are generally consistent with published τ_c^* values derived from channel slope and/or grain size, which typically range from 0.02 to 0.1 (Buffington & Montgomery, 1997), giving confidence to their application to reach-scale analysis.

Force-balance models incorporate additional grain-scale variabilities in bed resistance forces, resulting in variable τ_c^* estimates, both between different channels, as well as quantifying bed mobility variability within the sampled channel bed (i.e., sub-meter scales). This approach therefore gives an opportunity to explore the spatial and temporal controls on bed mobilities over large sample sizes. For example, this could assist in better understanding the processes involved in the de/re-stabilization cycles of channel beds in the field and in real-time. The incorporation of force-balance-estimated τ_c^* distributions, rather than values assumed solely from grain size and/or channel slope, would improve our ability to model sediment transfer between reaches, and could provide further insight into identifying likely hotspots of channel aggradation and degradation. Untangling relationships between grain size, slope and τ_c^* could be a valuable starting point toward refining sediment transport threshold variabilities over larger scales, for example, in landscape and channel evolution models (Coulthard & Macklin, 2001; Coulthard & Skinner, 2016; Temme et al., 2009, 2017). Furthermore, a better understanding of spatial variabilities in τ_c^* could be important in better predicting and managing future geomorphic hazards, such as bank erosion and flood risk.

The development of automated approaches for parameterizing the grain force-balance equations, for example, Pro+, enable faster collection of bed microtopography data, and produce estimated τ_c^* distributions with easily attainable point cloud data, and minimal post-processing analyses. As such, tools such as Pro+ are valuable in collecting large bed mobility data sets, over varying spatial scales, from reach to catchment scales. Critically, we find no notable trade-off between analysis speed and consistency of estimated τ_c^* between approaches. The relatively high consistency in estimated τ_c^* between both of the tested approaches, particularly for more mobile grains in the lower 50th percentile of the τ_c^* distribution, gives further confidence in the use of automated tools such as Pro+ in evaluating thresholds for the onset of sediment transport.

6. Conclusions and Recommendations

We critically evaluate two variations of grain force-balance models for estimating sediment mobility thresholds. First, a Monte Carlo style sampling approach utilizes manually sampled grain size, topography and force inputs collected in the field and through DEM analysis. Second, Pro+ estimates bed mobility thresholds using an updated set of force grain balance equations, incorporating grain data from automatically segmented point clouds. The automated approach produces τ_c^* values which are generally consistent with the Monte Carlo approach,

highlighting the value of Pro+ in collecting bed mobility estimates over large scales. We identify key uncertainties which likely lead to observed inconsistencies between the two approaches, and make the following comments and recommendations for their future applications.

1. Coarser grain size fractions exhibit systematically lower median τ_c^* than fine fractions, evidencing the role of grain hiding effects on particle mobility.
2. Grain size inputs can differ according to the sampling approach employed, and the accuracy of grain segmentation. We recommend additional validation of automated grain identification by manually collecting a GSD of the entire sample, and comparing it against GSD derived from the segmented point cloud, or by using novel machine learning approaches for grain segmentation. The relative influence of grain size bias on estimated τ_c^* , is difficult to isolate.
3. Methodologies for quantifying grain protrusion differ between studies. Pro+ offers a fast and consistent approach but is limited largely by the quality of grain segmentation.
4. Variabilities in bed roughness height and intergranular friction angle result in considerable changes in estimated τ_c^* . The degree of sensitivity is also influenced by grain size; finding a suitable assumption that suits all grains is therefore particularly difficult for poorly sorted samples.
5. In our application of Pro+, resistance force (F_R) is incorporated into τ_c^* estimates by adjusting the assumed intergranular friction angle to best match values measured in the field. We assume that ϕ_{fric} is equal for all grains in the sample but recommend adding a variability to sampled ϕ_{fric} values, to better constrain variability of grain resistance within samples; we offer groundwork sensitivity analysis for guidance.

Data Availability Statement

Data sets comprising gravel-bed microtopographies and field distributions for grain size, mass and resistance forces at each of the studied sites are available in the Zenodo repository (Whitfield et al., 2024).

Acknowledgments

This research was funded by NERC CENTA2 studentship (NE/S007350/1) to DW. Field data collection was supported by a British Society for Geomorphology postgraduate research grant awarded to DW. This work was also supported by NSF Grant (EAR1921790) awarded to EMY. We thank David Mair and two anonymous reviewers for their constructive feedback on this paper.

References

- Barzilai, R., Laronne, J. B., & Reid, I. (2013). Effect of changes in fine-grained matrix on bedload sediment transport in a gravel-bed river. *Earth Surface Processes and Landforms*, 38(5), 441–448. <https://doi.org/10.1002/esp.3288>
- Buffington, J. M., Dietrich, W. E., & Kirchner, J. W. (1992). Friction angle measurements on a naturally formed gravel streambed: Implications for critical boundary shear stress. *Water Resources Research*, 28(2), 411–425. <https://doi.org/10.1029/91WR02529>
- Buffington, J. M., & Montgomery, D. R. (1997). A systematic analysis of eight decades of incipient motion studies, with special reference to gravel-bedded rivers. *Water Resources Research*, 33(8), 1993–2029. <https://doi.org/10.1029/96WR03190>
- Bunte, K., & Abt, S. R. (2001). Sampling frame for improving pebble count accuracy in coarse gravel-bed streams. *Journal of the American Water Resources Association*, 37(4), 1001–1014. <https://doi.org/10.1111/j.1752-1688.2001.tb05528.x>
- Bunte, K., Abt, S. R., Swingle, K. W., Cenderelli, D. A., & Schneider, J. M. (2013). Critical Shields values in coarse-bedded steep streams. *Water Resources Research*, 49(11), 7427–7447. <https://doi.org/10.1002/2012WR012672>
- Butler, J. B., Lane, S. N., & Chandler, J. H. (2001). Automated extraction of grain-size data from gravel surfaces using digital image processing. *Journal of Hydraulic Research*, 39(5), 519–529. <https://doi.org/10.1080/00221686.2001.9628276>
- Caponi, F., & Siviglia, A. (2018). Numerical modeling of plant root controls on gravel bed river morphodynamics. *Geophysical Research Letters*, 45(17), 9013–9023. <https://doi.org/10.1029/2018GL078696>
- Chapman, W. A. L., Finnegan, N. J., Pfeiffer, A. M., & La Selle, S. P. (2021). River floodplain abandonment and channel deepening coincide with the onset of clear-cut logging in a coastal California redwood forest. <https://doi.org/10.1002/esp.5299>
- Church, M., Hassan, M. A., & Wolcott, J. F. (1998). Stabilizing self-organized structures in gravel-bed stream channels: Field and experimental observations. *Water Resources Research*, 34(11), 3169–3179. <https://doi.org/10.1029/98WR00484>
- Coulthard, T. J., & Macklin, M. G. (2001). How sensitive are river systems to climate and land-use changes? A model-based evaluation. *Journal of Quaternary Science*, 16(4), 347–351. <https://doi.org/10.1002/jqs.604>
- Coulthard, T. J., & Skinner, C. J. (2016). The sensitivity of landscape evolution models to spatial and temporal rainfall resolution. *Earth Surface Dynamics*, 4(3), 757–771. <https://doi.org/10.5194/esurf-4-757-2016>
- Di Francesco, S., Biscarini, C., & Manciola, P. (2016). Characterization of a flood event through a sediment analysis: The Tescio River case study. *Water*, 8(7), 308. <https://doi.org/10.3390/w8070308>
- Diplas, P., & Fripp, J. B. (1992). Properties of various sediment sampling procedures. *Journal of Hydraulic Engineering*, 118(7), 955–970. [https://doi.org/10.1061/\(asce\)0733-9429\(1992\)118:7\(955\)](https://doi.org/10.1061/(asce)0733-9429(1992)118:7(955))
- Downs, P. W., & Soar, P. J. (2021). Beyond stationarity: Influence of flow history and sediment supply on coarse bedload transport. *Water Resources Research*, 57(2), e2020WR027774. <https://doi.org/10.1029/2020wr027774>
- Dunne, K. B. J., & Jerolmack, D. J. (2020). What sets river width? *Science Advances*, 6(41), 1–9. <https://doi.org/10.1126/sciadv.abc1505>
- Eltner, A., Kaiser, A., Castillo, C., Rock, G., Neugirg, F., & Abellan, A. (2015). Image-based surface reconstruction in geomorphometry—Merits, limits and developments of a promising tool for geoscientists. *Earth Surface Dynamics Discussions*, 1445–1508. <https://doi.org/10.5194/esurf-d-3-1445-2015>
- Feehan, S. A., McCoy, S. W., Scheingross, J. S., & Gardner, M. H. (2023). Quantifying variability of incipient-motion thresholds in gravel-bedded rivers using a grain-scale force-balance model. *Journal of Geophysical Research: Earth Surface*, 128(9), e2023JF007162. <https://doi.org/10.1029/2023JF007162>

- Garefalakis, P., do Prado, A. H., Mair, D., Douillet, G. A., Nyffenegger, F., & Schlunegger, F. (2023). Comparison of three grain size measuring methods applied to coarse-grained gravel deposits. *Sedimentary Geology*, *446*, 106340. <https://doi.org/10.1016/j.sedgeo.2023.106340>
- Graham, D. J., Rice, S. P., & Reid, I. (2005). A transferable method for the automated grain sizing of river gravels. *Water Resources Research*, *41*(7), 1–12. <https://doi.org/10.1029/2004WR003868>
- Graham, D. J., Rollet, A.-J., Rice, S. P., & Piégay, H. (2012). Conversions of surface grain-size samples collected and recorded using different procedures. *Journal of Hydraulic Engineering*, *138*(10), 839–849. [https://doi.org/10.1061/\(asce\)hy.1943-7900.0000595](https://doi.org/10.1061/(asce)hy.1943-7900.0000595)
- Hodge, R. A., Sear, D. A., & Leyland, J. (2013). Spatial variations in surface sediment structure in riffle-pool sequences: A preliminary test of the differential sediment entrainment hypothesis (DSEH). *Earth Surface Processes and Landforms*, *38*(5), 449–465. <https://doi.org/10.1002/esp.3290>
- Hodge, R. A., Voepel, H., Leyland, J., Sear, D. A., & Ahmed, S. (2020). X-ray computed tomography reveals that grain protrusion controls critical shear stress for entrainment of fluvial gravels. *Geology*, *48*(2), 149–153. <https://doi.org/10.1130/G46883.1>
- Johnston, C. E., Andrews, E. D., & Pitlick, J. (1998). In situ determination of particle friction angles of fluvial gravels. *Water Resources Research*, *34*(8), 2017–2030. <https://doi.org/10.1029/98WR00312>
- Kirchner, J. W., Dietrich, W. E., Iseya, F., & Ikeda, H. (1990). The variability of critical shear stress, friction angle, and grain protrusion in water-worked sediments. *Sedimentology*, *37*(4), 647–672. <https://doi.org/10.1111/j.1365-3091.1990.tb00627.x>
- Lamb, M. P., Brun, F., & Fuller, B. M. (2017). Hydrodynamics of steep streams with planar coarse-grained beds: Turbulence, flow resistance, and implications for sediment transport. *Water Resources Research*, *53*(3), 2240–2263. <https://doi.org/10.1002/2016WR019579>
- Lamb, M. P., Dietrich, W. E., & Venditti, J. G. (2008). Is the critical Shields stress for incipient sediment motion dependent on channel-bed slope? *Journal of Geophysical Research*, *113*(F2), F02008. <https://doi.org/10.1029/2007JF000831>
- Mair, D., Witz, G., Do Prado, A. H., Garefalakis, P., & Schlunegger, F. (2024). Automated detecting, segmenting and measuring of grains in images of fluvial sediments: The potential for large and precise data from specialist deep learning models and transfer learning. *Earth Surface Processes and Landforms*, *49*(3), 1099–1116. <https://doi.org/10.1002/esp.5755>
- Mao, L. (2012). The effect of hydrographs on bed load transport and bed sediment spatial arrangement. *Journal of Geophysical Research*, *117*(3), F03024. <https://doi.org/10.1029/2012JF002428>
- Masteller, C. C., Finnegan, N. J., Turowski, J. M., Yager, E. M., & Rickenmann, D. (2019). History-dependent threshold for motion revealed by continuous bedload transport measurements in a steep mountain stream. *Geophysical Research Letters*, *46*(5), 2583–2591. <https://doi.org/10.1029/2018GL081325>
- Métivier, F., Lajeunesse, E., & Devauchelle, O. (2017). Laboratory rivers: Lacey’s law, threshold theory, and channel stability. *Earth Surface Dynamics*, *5*(1), 187–198. <https://doi.org/10.5194/esurf-5-187-2017>
- Ockelford, A., Woodcock, S., & Haynes, H. (2019). The impact of inter-flood duration on non-cohesive sediment bed stability. *Earth Surface Processes and Landforms*, *44*(14), 2861–2871. <https://doi.org/10.1002/esp.4713>
- Parker, G., Wilcock, P. R., Paola, C., Dietrich, W. E., & Pitlick, J. (2007). Physical basis for quasi-universal relations describing bankfull hydraulic geometry of single-thread gravel bed rivers. *Journal of Geophysical Research*, *112*(4), F04005. <https://doi.org/10.1029/2006JF000549>
- Pfeiffer, A. M., Finnegan, N. J., & Willenbring, J. K. (2017). Sediment supply controls equilibrium channel geometry in gravel rivers. *Proceedings of the National Academy of Sciences of the United States of America*, Vol. 114(13), 3346–3351. <https://doi.org/10.1073/pnas.1612907114>
- Phillips, C. B., Masteller, C. C., Slater, L. J., Dunne, K. B. J., Francalanci, S., Lanzoni, S., et al. (2021). The importance of threshold in alluvial river channel geometry and dynamics. Retrieved from <http://eartharxiv.org/repository/view/2400/>
- Prancevic, J. P., & Lamb, M. P. (2015). Particle friction angles in steep mountain channels. *Journal of Geophysical Research: Earth Surface*, *120*(2), 242–259. <https://doi.org/10.1002/2014JF003286>
- Qin, J., Aberle, J., Henry, P. Y., Wu, T., & Zhong, D. (2019). Statistical significance of spatial correlation patterns in armoured gravel beds. *Journal of Hydraulic Research*, *57*(1), 90–106. <https://doi.org/10.1080/00221686.2018.1459894>
- Qin, J., & Ng, S. L. (2012). Estimation of effective roughness for water-worked gravel surfaces. *Journal of Hydraulic Engineering*, *138*(11), 923–934. [https://doi.org/10.1061/\(ASCE\)HY.1943-7900.0000610](https://doi.org/10.1061/(ASCE)HY.1943-7900.0000610)
- Recking, A. (2009). Theoretical development on the effects of changing flow hydraulics on incipient bed load motion. *Water Resources Research*, *45*(4), W04401. <https://doi.org/10.1029/2008WR006826>
- Recking, A. (2010). A comparison between flume and field bed load transport data and consequences for surface-based bed load transport prediction. *Water Resources Research*, *46*(3), W03518. <https://doi.org/10.1029/2009WR008007>
- Recking, A. (2012). Influence of sediment supply on mountain streams bedload transport. *Geomorphology*, *175–176*, 139–150. <https://doi.org/10.1016/j.geomorph.2012.07.005>
- Sanguinito, S., & Johnson, J. (2012). Quantifying gravel overlap and dislodgement forces on natural river bars: Implications for particle entrainment. *Earth Surface Processes and Landforms*, *37*(1), 134–141. <https://doi.org/10.1002/esp.2237>
- Sime, L. C., & Ferguson, R. I. (2003). Information on grain sizes in gravel-bed rivers by automated image analysis. *Journal of Sedimentary Research*, *73*(4), 630–636. <https://doi.org/10.1306/112102730630>
- Slater, L. J., Khouakhi, A., & Wilby, R. L. (2019). River channel conveyance capacity adjusts to modes of climate variability. *Scientific Reports*, *9*(1), 1–10. <https://doi.org/10.1038/s41598-019-48782-1>
- Slater, L. J., Singer, M. B., & Kirchner, J. W. (2015). Hydrologic versus geomorphic drivers of trends in flood hazard. *Geophysical Research Letters*, *42*(2), 370–376. <https://doi.org/10.1002/2014GL062482>
- Smith, H. E. J., Monsalve, A. D., Turowski, J. M., Rickenmann, D., & Yager, E. M. (2023). Controls of local grain size distribution, bed structure and flow conditions on sediment mobility. *Earth Surface Processes and Landforms*, *48*(10), 1990–2004. <https://doi.org/10.1002/esp.5599>
- Steer, P., Guérit, L., Lague, D., Crave, A., & Gourdon, A. (2022). Size, shape and orientation matter: Fast and automatic measurement of grain geometries from 3D point clouds (pp. 1–31).
- Temme, A. J. A. M., Armitage, J., Attal, M., van Gorp, W., Coulthard, T. J., & Schoorl, J. M. (2017). Developing, choosing and using landscape evolution models to inform field-based landscape reconstruction studies. In *Earth surface processes and landforms* (pp. 2167–2183). John Wiley and Sons Ltd. <https://doi.org/10.1002/esp.4162>
- Temme, A. J. A. M., Baartman, J. E. M., & Schoorl, J. M. (2009). Can uncertain landscape evolution models discriminate between landscape responses to stable and changing future climate? A millennial-scale test. *Global and Planetary Change*, *69*(1–2), 48–58. <https://doi.org/10.1016/j.gloplacha.2009.08.001>
- Turowski, J. M., Badoux, A., & Rickenmann, D. (2011). Start and end of bedload transport in gravel-bed streams. *Geophysical Research Letters*, *38*(4), L04401. <https://doi.org/10.1029/2010GL046558>
- Venditti, J. G., Dietrich, W. E., Nelson, P. A., Wydzga, M. A., Fadde, J., & Sklar, L. (2010). Effect of sediment pulse grain size on sediment transport rates and bed mobility in gravel bed rivers. *Journal of Geophysical Research*, *115*(3), F03039. <https://doi.org/10.1029/2009JF001418>

- Voepel, H., Leyland, J., Hodge, R. A., Ahmed, S., & Sear, D. (2019). Development of a vector-based 3D grain entrainment model with application to X-ray computed tomography scanned riverbed sediment. *Earth Surface Processes and Landforms*, *44*(15), 3057–3077. <https://doi.org/10.1002/esp.4608>
- Whitfield, D., Baynes, E., & Rice, S. (2024). Gravel-bed mobilities and microtopographies for streams across England and Wales (version 1) [Dataset]. *Zenodo*. <https://doi.org/10.5281/zenodo.13323710>
- Whiting, P. J., & Dietrich, W. E. (1990). Boundary shear stress and roughness over mobile alluvial beds. *Journal of Hydraulic Engineering*, *116*(12), 1495–1511. [https://doi.org/10.1061/\(ASCE\)0733-9429\(1990\)116:12\(1495\)](https://doi.org/10.1061/(ASCE)0733-9429(1990)116:12(1495))
- Wiberg, P. L., & Smith, J. D. (1987). Calculations of the critical shear stress for motion of uniform and heterogeneous sediments. *Water Resources Research*, *23*(8), 1471–1480. <https://doi.org/10.1029/WR023i008p01471>
- Wilcock, B. P. R. (1993). Critical shear stress of natural sediments. *Journal of Hydraulic Engineering*, *119*(4), 491–505. [https://doi.org/10.1061/\(asce\)0733-9429\(1993\)119:4\(491\)](https://doi.org/10.1061/(asce)0733-9429(1993)119:4(491))
- Yager, E. M., Kirchner, J. W., & Dietrich, W. E. (2007). Calculating bed load transport in steep boulder bed channels. *Water Resources Research*, *43*(7), W07418. <https://doi.org/10.1029/2006WR005432>
- Yager, E. M., Schmeeckle, M. W., & Badoux, A. (2018). Resistance is not futile: Grain resistance controls on observed critical shields stress variations. *Journal of Geophysical Research: Earth Surface*, *123*(12), 3308–3322. <https://doi.org/10.1029/2018JF004817>
- Yager, E. M., Shim, J., Hodge, R., Monsalve, A., Tonina, D., Johnson, J. P. L., & Telfer, L. (2024). Pro+: Automated protrusion and critical shear stress estimates from 3D point clouds of gravel beds. *Earth Surface Processes and Landforms*, *49*(7), 2155–2170. <https://doi.org/10.1002/esp.5822>